HHS Public Access

Author manuscript

Biochem J. Author manuscript; available in PMC 2021 July 14.

Published in final edited form as:

Biochem J. ; 475(6): 1211–1223. doi:10.1042/BCJ20180016.

Heme degradation enzyme biliverdin IXβ reductase is required for stem cell glutamine metabolism

Zongdong Li[1,2], **Natasha M. Nesbitt**[1], **Lisa E. Malone**[1], **Dimitri V. Gnatenko**[1], **Song Wu**[3], **Daifeng Wang**[4], **Wei Zhu**[3], **Geoffrey D. Girnun**[5], **Wadie F. Bahou**[1]

[1]Department of Medicine, Stony Brook University, Stony Brook, NY 11794, U.S.A.

[2]Department of Medicine and the Stony Brook Stem Cell Facility, Stony Brook University School of Medicine, Stony Brook, NY 11794-6044, U.S.A.

[3]Department of Applied Mathematics and Statistics, Stony Brook University, Stony Brook, NY 11794, U.S.A.

[4]Department of Biomedical Informatics, Stony Brook University, Stony Brook, NY 11794, U.S.A.

[5]Department of Pathology, Stony Brook University, Stony Brook, NY 11794, U.S.A.

Abstract

Bioenergetic requirements of hematopoietic stem cells and pluripotent stem cells (PSCs) vary with lineage fate, and cellular adaptations rely largely on substrate (glucose/glutamine) availability and mitochondrial function to balance tricarboxylic acid (TCA)-derived anabolic and redox-regulated antioxidant functions. Heme synthesis and degradation converge in a linear pathway that utilizes TCA cycle-derived carbon in cataplerotic reactions of tetrapyrrole biosynthesis, terminated by NAD(P)H-dependent biliverdin reductases (IXα, BLVRA and IXβ, BLVRB) that lead to bilirubin generation and cellular antioxidant functions. We now demonstrate that PSCs with targeted deletion of *BLVRB* display physiologically defective antioxidant activity and cellular viability, associated with a glutamine-restricted defect in TCA entry that was computationally predicted using gene/metabolite topological network analysis and subsequently validated by bioenergetic and isotopomeric studies. Defective BLVRB-regulated glutamine utilization was accompanied by exaggerated glycolytic accumulation of the rate-limiting hexokinase reaction product glucose-6-phosphate. *BLVRB*-deficient embryoid body formation (a critical size parameter of early lineage fate potential) demonstrated enhanced sensitivity to the pentose phosphate pathway (PPP) inhibitor 6-aminonicotinamide with no differences in the glycolytic pathway inhibitor 2-deoxyglucose. These collective data place heme catabolism in a crucial pathway of glutamine-regulated bioenergetic metabolism and suggest that early stages of lineage fate potential require glutamine anaplerotic functions and an intact PPP, which are, in part, regulated by BLVRB activity. In

Correspondence: Zongdong Li (zongdong.li@stonybrookmedicine.edu).

Author Contribution

Z.L. and W.F.B. conceptualized this study. Z.L., S.W., D.W., W.Z., G.D.G., and W.F.B. performed methodology of this work. L.E.M., D.V.G., and N.M.N. investigated this study. Z.L. and W.F.B. involved in writing the original draft and review and editing. N.M.N., D.V.G., G.D.G., and W.F.B. acquired funding of this work. Z.L., G.D.G., and W.F. B. collected resources for this work. Z.L., G.D.G., and W.F.B. supervised this study.

Competing Interests

The Authors declare that there are no competing interests associated with the manuscript.

principle, BLVRB inhibition represents an alternative strategy for modulating cellular glutamine utilization with consequences for cancer and hematopoietic metabolism.

Introduction

Bioenergetic requirements of hematopoietic stem cells (HSCs) and pluripotent stem cells (PSC) vary with lineage fate, and cellular adaptations rely largely on substrate (glucose/glutamine) availability and mitochondrial function to balance TCA (tricarboxylic acid)-derived anabolic requirements, redox homeostasis, and reactive oxygen species (ROS) [1]. These adaptations are especially relevant to PSCs which maintain a balance between metabolically quiescent, non-cycling (ROS^{low}) cells in the hypoxic bone marrow niche and a metabolically active (ROS^{high}) phenotype associated with the switch to aerobic (oxidative phosphorylation) metabolism and proliferation. ROS accumulation promotes lineage-restricted hematopoietic development [2], although ROS generation exceeding the capacity of cellular antioxidant mechanisms promotes senescence and apoptosis. Mitochondria and NADPH oxidase are the primary sources of ROS generation [3], and oxidation of glucose and glutamine via the mitochondrial TCA cycle provides the critical source of biosynthetic precursors required for cellular proliferation. Quiescent stem cells largely depend on glycolysis for ATP synthesis, and glutamine oxidation is indispensable for survival of PSCs [4], serves as a crucial mitochondrial substrate for cancer cells [5], and regulates human HSC lineage specification [6]. Similarly, since the NAD^+/NADH ratio is regulated by glycolytic and mitochondrial activities that change dramatically during differentiation or reprogramming [7], the NAD^+/NADH redox state may have a role in driving PSC fate.

Heme (protoporphyrin IX complexed with iron) serves as an indispensable cofactor for all aerobic cells, providing the prosthetic group for phylogenetically distinct hemoproteins functioning in the electron transport chain (ETC), gas exchange, or as light-sensing plant or bacterial phytochromes [8]. Heme biosynthesis is initiated by the condensation of TCA-derived succinyl CoA and glycine, whose generation from serine provides 1-carbon units coupled to the folate cycle for purine and thymidine biosynthesis [9]. The cytotoxicity of free heme is minimized by a two-step catabolic reaction initiated by heme oxygenases (HMOX1 and HMOX2), with sequential generation of biliverdin (BV) and bilirubin (BR) tetrapyrroles in a major pathway functioning in cellular defenses against oxidative and nitrosative stress [10,11]. BV to BR derivatization is regulated by two non-redundant BV reductases (BLVRA and BLVRB), differing by their isomeric specificity in NAD(P) H-dependent oxidation/reduction (redox) coupling. BLVRA retains specificity for the predominant BV found in adults (BVIXα) with less efficient utilization of BV IXβ, IXγ, or IXδ [12,13], while BLVRB is promiscuous, catalyzing the NAD(P)H-dependent reduction of non-IXα BVs [14], several flavins [15], and pyrroloquinoline quinones [16]. Thus, heme synthesis and degradation converge in a linear pathway that utilizes TCA cycle-derived carbon in cataplerotic reactions ultimately linked to BR generation and cellular antioxidant functions [17].

Preferential reliance on glycolytic pathways is a common bioenergetic feature of PSC and cancer metabolism despite low efficient ATP generation [1,5], and both PSCs and cancer

cells reside in hypoxic niches and rely on glutamine metabolism for survival and growth [4,5]. The overlapping glucose/glutamine requirements for both heme biosynthesis and PSC substrate utilization suggested that dysregulated heme metabolism would affect bioenergetic utilization. We focused on BLVRB because of its acknowledged activity in early fetal development [14], coupled with recent evidence for a redox-regulated function governing hematopoietic lineage fate [18].

Materials and methods

Materials

All regents were of the highest purity commercially available. BV was purchased from Frontier Scientific, Inc. (Logan, UT); BR, NADPH, and FMN (flavin mononucleotide) were purchased from Sigma–Aldrich. High-performance liquid chromatography (HPLC) grade acetonitrile, methanol, and water were purchased from Burdick & Jackson (Morristown, NJ).

Bioethical studies using induced PSCs

Studies using induced PSCs were approved by the Stony Brook IRB (Institutional Review Board) in accordance with the Declaration of Helsinki [19].

Genome editing in PSCs

Induced PSCs derived from $CD34^+$ human umbilical cords (NCRM1) were obtained from the NIH Center for Regenerative Medicine and propagated on matrigel-coated surfaces under normoxic conditions in feeder- and serum-free cell culture medium (mTeSR, Stem Cell Technologies, Vancouver, BC). Single-guide RNA (sgRNA) oligonucleotides were designed using the clustered regularly interspaced short palindromic repeats (CRISPR) Design Tool (http://crispr.mit.edu/) to minimize off-target effects and selected to precede a 5′-NGG protospacer-adjacent motif (PAM). sgRNAs used in the present study were synthesized to target *BLVRB* exon 3 nucleotides 430–449 (RefSeq ID NM_000713.2) contiguous to Serine 111, sequence as follows: sgRNA1: 5′-TCATGGTGTGGACAAGGTCG-3′; control sgRNA: 5′-GTAGCGAACGTGTCCGGCGT-3′. Oligonucleotides were annealed and cloned into the *BbsI* site of the *Streptococcus pyogenes* Cas9 (SpCas9) nuclease (plasmid PX458; Addgene, Cambridge, MA), thereby allowing for transfection monitoring using green fluorescent protein (GFP) detection. NCRM1 transfection was completed using Lipofectamine 3000 (Life Technologies), and GFP^+ cells were sorted and collected by flow cytometry for expansion and further characterization. Putative off-target effects were excluded by RNASeq and detailed sequence alignments of the top 50 sites predicted for the guide sequence (http://crispr.mit.edu).

PSC growth curves and embryoid body formation

PSCs plated at a density of 5×10^3 cells/well were propagated in mTesR media and harvested at specific time points using Accutase (Innovative Cell Technologies) for quantification. Phosphatidylserine-expressing (apoptotic) cells were detected using 5 μl Annexin-V-FITC for 15 min at 25°C in the dark. Samples (both counts and Annexin V-

positivity) were immediately analyzed using a BD LSRFortessa flow cytometer (BD Biosciences) using the 488 nm laser to detect Annexin-V-FITC (490/525 nm), or absolute cell quantification using a fixed flow rate of 100 μl/min. The effect of 2-deoxyglucose (2-DG, Sigma–Aldrich) or 6-AN (6-aminonicotinamide, Cayman Chemical) on cell growth was evaluated in an identical fashion, modified for supplementation at 2-day intervals. Embryoid bodies (EBs) were generated and quantified as previously described [20]. Briefly, cells were initially dissociated using Accutase (Stem Cell Technologies), followed by pelleting and resuspension in mTeSR medium containing 10 μM ROCK inhibitor (R&D Systems) and various concentrations (or not) of 6-AN or 2-DG. Viable cells were counted using trypan blue exclusion and equivalent numbers (1×10^5 cells) were plated by gentle centrifugation (300×***g*** for 3 min) into AggreWell plates (Stem Cell Technologies), followed by 37°C incubation to allow for EB formation. EB formation was confirmed by immunofluorescence staining using the pluripotency marker Oct3/4 (R&D Systems); quantification and microscopic visualization were completed at Day 3, and individual EB size was quantified using the Image J software.

Biostatistics

Statistical comparisons were completed using ANOVA or *t*-test, modified for bootstrap resampling to compare relative EB size change in the presence of 6-AN; for all comparisons, a value of $P < 0.05$ was applied for establishing statistical significance.

Details of other experimental procedures are described in Supplementary Materials and Methods.

Results

Generation of *BLVRB*-deficient (*BLVRB*$^{-/-}$) PSCs

Targeted *BLVRB* disruption in PSCs was completed by genome editing using PSCs derived from human umbilical cord CD34$^+$ hematopoietic cells (Figure 1A and Supplementary Figure S1). The guide RNA (gRNA) strand (or control gRNA) designed to target *BLVRB* exon 3 contiguous to the active-site serine^{111} [21] was introduced into a plasmid encoding the single-strand nickase Cas9n and GFP, followed by flow cytometric enrichment of GFP$^+$ cells. Sequence analysis of six expanded subclones confirmed the presence of distinct exon 3 mutations, and two independent subclones (*BLVRB*$^{-/-CL19}$ and *BLVRB*$^{-/-CL20}$) encompassing a 6-bp *BLVRB* deletion had no evidence for genetic aberrations (in/dels) as established both by RNASeq and focused off-target prediction algorithms [22]. Unsupervised hierarchical clustering using the limited subset of differentially expressed genes ($N = 42$, P-value < 0.001 to minimize false discovery rate) confirmed genetic co-segregation of both *BLVRB*$^{-/-}$ PSCs from either naive or control PSCs (Figure 1B and Supplementary Figure S1). Only two genes (*HIST1H4F* and *MAGEA4*) displayed >2-fold difference between *BLVRB*$^{-/-CL19}$ and *BLVRB*$^{-/-CL20}$ (Supplementary Table S1); importantly, both *BLVRB*$^{-/-CL19}$ and *BLVRB*$^{-/-CL20}$ demonstrated concordant down-regulation of both *HIST1H4F* (~67-fold) and *MAGEA4* (~40-fold) compared with control and naive iPSCs, establishing the relative genetic homogeneity compared with control or naive iPSCs.

Immunoblot analysis confirmed the absence of BLVRB protein in both clones, with no evidence that *BLVRB*-deficient PSCs had reciprocal induction of BLVRA protein or enzymatic activity (Figure 1C,D). HMOXs have potent effects on regulation of cellular integrity and function, and we confirmed that *BLVRB*-deficient PSCs had no statistically significant alterations in inducible *HMOX1* or constitutive *HMOX2* transcripts (Figure 1E). Similarly, flow cytometric analyses using pluripotency markers Tra-1–60 and SSEA4 were nearly identical between the genotypes, with modest loss of SSEA3 and CD117 (c-Kit proto-oncogene) in *BLVRB*-deficient PSCs (more evident in $BLVRB^{-/-CL20}$); nonetheless, there was no evidence for exaggerated differentiation as established using KDR (vascular endothelial growth factor receptor 2) as the hemato-endothelial marker (Supplementary Figure S1).

BLVRB maintains a requisite function in PSC oxidant neutralization

Both BVs and BRs retain signaling and metabolic functions [12,13] and a BV–BR redox cycle has been proposed as an amplifiable potent buffer against ROS and oxidant stress [10,11]. Virtually, all mammalian BVs are generated by regioselective cleavage at the α-meso carbon (BV IXα) [14], and across the genotypes, we were unable to detect secreted BV IXβ isomers in any of the samples [sensitivity 1 ng/μl, although secreted BV IXα isomers were readily detectable and similar across all PSCs (Figure 1F)]. Thus, PSCs (like adult tissues) appear to have limited capacity for non-BV IXα generation under steady-state conditions [21]. Immunofluorescent microscopy using a cell-permeant fluorogenic probe to quantify ROS in live cells demonstrated exaggerated ROS accumulation in both $BLVRB^{-/-CL19}$ and $BLVRB^{-/-CL20}$ compared with control PSCs (Figure 1G). The greatest ROS accumulation was most evident along the metabolically active cellular leading edge, although a statistically significant increase was evident throughout the culture in both $BLVRB^{-/-}$ PSCs. Defective ROS handling was associated with time-dependent loss of cell number in both $BLVRB^{-/-CL19}$ and $BLVRB^{-/-CL20}$ PSCs compared with control (Figure 1H), results which were largely accounted for by apoptotic cell death as documented by cell-surface phosphatidylserine exposure using Annexin V binding (Figure 1I). These collective data established that BLVRB maintained a physiologically significant and requisite role in metabolic regulation of PSC antioxidant homeostasis and cellular viability. The lack of identifiable defects affecting isomeric BV IXα/IXβ accumulation suggested that the mechanism(s) leading to these phenotypic differences extended beyond those directly associated with BLVRB-dependent redox coupling.

Perturbed metabolic networks in *BLVRB*-deficient PSCs

Since interconnected metabolic networks are highly adaptive to single-gene perturbations [17], we developed a genome-scale systems biology approach to better delineate pathway perturbations causally implicated in *BLVRB*-deficient bioenergetic responses. Across the genotypes, we quantified the steady-state accumulation of 290 intracellular metabolites using multiple reaction monitoring and microcapillary liquid chromatography/tandem mass spectrometry (LC–MS/MS, $N = 6$ determinations/genotype) and applied the Pearson correlation coefficient (r) to sequentially identify BLVRB-associated metabolites across the PSCs ($r \geq 0.8$), followed by a similar approach to identify the genetic subset ($r \geq 0.8$) correlated with at least one of these metabolites (Figure 2A). Hierarchical clustering of this

extended correlation matrix ($N = 45$ metabolites and 1932 genes) delineated gene/metabolite pairs co-segregating into three predominant biclusters ($P < 2.2 \times 10^{-16}$), whose metabolic enrichment and topological pathway analyses identified a limited number of perturbed pathways ($N = 9$ using $P < 0.05$), collectively involved in nucleotide biosynthesis (purine and pyrimidine), redox homeostasis (pentose phosphate pathway [PPP]), and bioenergetics/biosynthesis (TCA cycle) (Figure 2B and Supplementary Table S2). Delineation of biological connectivity was further elucidated by constructing a comprehensive network encompassing the gene/metabolite subsets (Figure 2C). The resulting network self-organized into distinct metabolic modules centrally anchored by BLVRB. Near-neighbor connectivity was closest for the known BLVRB substrate FMN [12], along with one TCA cycle intermediate fumarate and maleic acid (hydrogenated succinic acid).

The collective pathway topology and network structure placed BLVRB at the intersection of converging pathways that utilize glucose and glutamine for biosynthesis and bioenergetics, along with the maintenance of cellular reducing capacity via PPP-mediated glycolysis. Indeed, while glycolytic entry into the oxidative component of the PPP maintains redox homeostasis by generating NAD(P)H reducing equivalents, the downstream non-oxidative branch of the cycle generates ribose-5-phosphate, the essential nucleotide component used for purine/pyrimidine synthesis and riboneogenesis [23]. Comparison of glycolytic metabolites across the genotypes confirmed nearly 9-fold accumulation of glucose-6-phosphate (G6P) in *BLVRB*$^{-/-}$ PSCs compared with control PSCs ($P < 1 \times 10^{-5}$), associated with statistically decreased levels of all downstream glycolytic metabolites (Figure 2D). G6P maintains the intracellular glucose pool, and its generation by the rate-limiting hexokinase reaction has been implicated in the switch to aerobic glycolysis that occurs during pluripotency reprogramming [24], consistent with a phenotypic switch of exaggerated glucose utilization in *BLVRB*$^{-/-}$ PSCs. Similar but less dramatic statistically different metabolic changes were evident in *BLVRB*$^{-/-}$ PPP (three of seven metabolites) and TCA (3 of 10 metabolites) pathways (Figure 2D), two of which (α-ketoglutarate and succinyl CoA) have roles in the maintenance of stem cell pluripotency [25]. Furthermore, while the $NADP^+$/NADPH and glutathione (reduced/oxidized) ratios were unchanged across the genotypes, *BLVRB*$^{-/-}$ PSCs demonstrated a diminished NAD^+/NADH ratio (Figure 2E–G), results collectively suggest a discrete bioenergetics defect with an adaptive glycolytic phenotype.

BLVRB$^{-/-}$ PSCs have a bioenergetic defect involving mitochondrial function and the ETC

The TCA cycle provides the primary source of mitochondrial NADH for the ETC and cellular respiration, prompting more detailed evaluation of mitochondrial function. MitoTracker green fluorescence demonstrated no obvious differences across the PSCs (Figure 3A), results which were extended using cell-permeant TMRE (tetramethylrhodamine ethyl ester) fluorescence as a functional marker of the mitochondrial transmembrane potential ($\Delta\Psi m$). Across the PSCs, we saw no evidence that substrate (i.e. glucose [Glc] or glutamine [Gln]) restriction affected TMRE fluorescence; furthermore, mitochondrial depolarization using the protonophore carbonyl cyanide *m*-chlorophenyl hydrazine (CCCP) was identical across all the PSCs, results collectively excluding a discrete mitochondrial defect exacerbated by substrate availability. We then compared basal and maximal oxygen consumption rates (OCRs) across the PSCs, modified for the presence or absence of Glc or

Gln as primary TCA anaplerotic substrate(s). In the absence of either substrate, basal (oligomycin-sensitive) OCRs were similar, confirming that the rate of respiration used to drive ATP synthesis was stable across the PSCs (Figure 3B). These results contrasted to those using Gln as the primary fuel, wherein control PSCs displayed an increased OCR that was blunted or diminished in both *BLVRB*$^{-/-CL19}$ and *BLVRB*$^{-/-CL20}$ PSCs. Across the genotypes, the availability of both Gln + Glc rescued the Gln response, confirming preferential and sufficient utilization of Glc for basal bioenergetics [1]. Since basal OCRs do not adequately reflect PSC response to situations of increased energy demand, we determined protonophore (FCCP, carbonyl cyanide-*p*-trifluoromethoxyphenylhydrazone)-stimulated respiration as a measure of mitochondrial substrate oxidation and maximal respiratory capacity [26]. In the absence of either substrate (–Gln, –Glc), both *BLVRB*$^{-/-CL19}$ and *BLVRB*$^{-/-CL20}$ PSCs displayed defective maximal OCRs, with a persistent defect in Gln-mediated OCRs compared with control PSCs (most pronounced in *BLVRB*$^{-/-CL20}$ PSCs); across the genotypes, Glc supplementation rescued the Gln defect (Figure 3C). Defective Gln-mediated basal and maximal OCRs were consistent with bioenergetic uncoupling of ATP synthesis and oxygen consumption [27], results which were underscored by striking loss of Gln-mediated proton leaklinked respiration in *BLVRB*$^{-/-CL19}$ and *BLVRB*$^{-/-CL20}$ PSCs (Figure 3D). These collective analyses were most consistent with a discrete defect involving Gln entry into the TCA cycle as the primary bioenergetics defect, largely (if not fully) reversible in the presence of Glc supplementation under either basal or maximal conditions.

Defective glutamine TCA entry in *BLVRB*$^{-/-}$ PSCs

Glutamine retains key metabolic functions by donating its nitrogen and carbon into various growth-promoting pathways [28], while its oxidation to α-ketoglutarate (α-KG) provides for TCA entry with effects on PSC maintenance [25] and survival [4] (Figure 4A). Metabolic flux quantification using [U-$^{13}C_5$] glutamine demonstrated nearly identical fractional uptake between control and *BLVRB*$^{-/-}$ PSCs, with comparable fractional labeling (and conversion) to [U-$^{13}C_5$] glutamate (Figure 4B). These results sharply contrasted to glutamate-derived α-KG where both *BLVRB*$^{-/-CL19}$ and *BLVRB*$^{-/-CL20}$ demonstrated statistically significant decreased accumulation of M +5 (i.e. labeled) isotopomers with decreased M+0 (endogenous) isotopomer in *BLVRB*$^{-/-CL19}$. Expectedly, diminished α-KG availability resulted in decreased accumulation of downstream metabolites fumarate and malate (M+0 and M+4) isotopomers with diminished succinate M+4 in *BLVRB*$^{-/-CL20}$ (Figure 4D–G), results confirming the presence of a discrete Gln defect in TCA entry and rewired glutamate metabolism. In contrast, basal metabolic flux using [U_6-^{13}C] glucose revealed high-level and comparable (>97%) fractional labeling of ^{13}C lactate across the genotypes (Figure 4G), confirming an intact and saturated glycolytic metabolism that was comparable between control and *BLVRB*$^{-/-}$ PSCs and unaffected by defective TCA glutamine entry.

BLVRB maintains PPP integrity during EB formation

Defective glutamate TCA entry suggested that the metabolic requirements of *BLVRB*$^{-/-}$ PSCs were adapted for differential glucose utilization, either for bioenergetics through the glycolytic pathway or for NAD(P)H reductive capacity and ribosylated nucleotides through PPP. In the presence of the glycolytic pathway inhibitor 2-DG or the PPP pathway inhibitor

6-AN (a 6-phosphogluconate dehydrogenase inhibitor [29]), both control and *BLVRB*$^{-/-}$ PSCs demonstrated comparable dose-dependent growth inhibition (Figure 5A,B), results highlighting a requisite role for both pathways in cell growth independent of BLVRB expression and glutamate anaplerotic functions. We then compared these results with EB three-dimensional aggregate formation, a definable endpoint of early ES cell differentiation that recapitulates embryonic gastrulation and functions as a critical size parameter of lineage fate potential [30,31]. In the absence of any inhibitors, *BLVRB*$^{-/-CL19}$ and *BLVRB*$^{-/-CL20}$ EBs displayed smaller size distributions compared with control EBs, establishing a requisite role for BLVRB-dependent glutamine anaplerotic functions in molecular regulation of early lineage fate potential (Figure 5C). Furthermore, 2-DG supplementation at a concentration (0.5 mM) maintaining >75% fractional growth survival in suspension cultures across the genotypes had a profound effect on EB formation (Figure 5D), inhibiting EB formation across the genotypes and establishing a requisite role for the glycolytic pathway in EB lineage fate potential unrelated to glutamine TCA entry. In contrast, 50 μM 6-AN which results in complete inhibition of cell growth across the genotypes in suspension culture (*vide supra*) did not inhibit EB formation; rather, 6-AN supplementation modulated EB size distribution across the genotypes, with an exaggerated effect on both *BLVRB*$^{-/-}$ PSCs (Figure 5C,D). Indeed, whereas the relative percent size changes for *BLVRB*$^{-/-CL19}$ and *BLVRB*$^{-/-CL20}$ in the presence of 6-AN supplementation are not significantly different, the percent change in each is significantly greater than control (*P*-value < 0.000001), confirming exaggerated 6-AN sensitivity across both *BLVRB*$^{-/-}$ PSCs. Both 6-AN and 2-DG pathway inhibitor effects were readily evident by the microscopic appearance of *BLVRB*$^{-/-}$ EBs, with dissolution of EB formation in the presence of 2-DG and morphologically smaller and less compact EB structure with 6-AN supplementation.

Discussion

Our data establish that PSCs require BLVRB reductase activity for physiologically relevant antioxidant activity and cellular viability, accompanied by a bioenergetics defect with diminished glutamate TCA entry. Dysregulated TCA glutamine utilization in *BLVRB*-deficient PSCs links heme generation and degradation with anaplerotic entry into the TCA cycle. TCA-derived succinate functions as one component (with glycine) of the rate-limiting ALAS (aminolevulinic acid synthase) reaction catalyzing the first step of tetrapyrrole biosynthesis and presumably explains the shunted glutamine response as an adaptive means of limiting heme generation. Secondary effects would lead to decreased ETC proteins (many of which functionalize with heme), acquired ETC defects with ROS accumulation [3], and dysfunctional TCA cycle NAD^+/NADH generation. Shunted glutamine was confirmed by isotopomeric tracings at the initial TCA entry point (α-ketoglutarate) and resulted in glutamine-restricted defects in oxygen consumption under both basal and maximal respiration.

These data are consistent with those previously demonstrating the critical role of heme generation/degradation pathways in rescuing the phenotype of the TCA cycle enzyme fumarate hydratase (FH) [17]. FH deficiency leads to truncation of the TCA cycle, fumarate accumulation, and hereditary leiomyomatosis and renal cell cancer [32]; the extended (glutamine to BR) heme generation/degradation pathway enables *FH*-deficient cells to use

accumulated TCA cycle metabolites as the carbon source and for partial mitochondrial NADH production [17]. Indeed, genetic adaptations of *FH*-deficient cells specifically demonstrate dysregulated *BLVRB* expression to the exclusion of any effects on *BLVRA*, an observation that underscores the crucial role of BLVRB reductase activity in bioenergetic metabolism linked to glutamine oxidation and TCA activity. Approaches directed at limiting glutamine utilization have been proposed as strategies for cancer therapeutics and for preparation of purified sources of terminally committed cells free of undifferentiated PSCs [4]; in theory, the shunted glutamine metabolism in BLVRB-*deficient* PSCs suggests an alternative approach of modulating cellular glutamine utilization by inhibiting BLVRB activity [33,34].

Loss of antioxidant function in $BLVRB^{-/-}$ PSCs is consistent with previously reported functions for BLVRA in various cell lines [11,35]. Unlike the BLVRA homolog whose pleiotropic cellular effects are mediated by multidomain features [36], BLVRB structure is generally featureless with a function (and therefore an antioxidant effect) presumably limited to its substrate/NAD(P)H redox activity [14]. Nonetheless, $BLVRB^{-/-}$ PSCs retain normal BLVRA activity, display no differential accumulation of BV IXα isomers, and undetectable BV Ixβ isomers, supporting the working model that BLVRB's antioxidant function occurs (in part) independently of its redox activity, and partially (if not fully) by a requisite function in TCA glutamate entry. Indeed, despite the enrichment of non-BV (BR) Ixα isomers (i.e. IXβ, IXγ, and IXδ) in early fetal development [37], identification of these isomers is rare in mammals and largely restricted to distinct HMOX variants found in bacteria such as *Pseudomonas aeruginosa* [38]. When integrated with our data, generation of these isomers appears to occur during a later (committed) stage of embryogenic development beyond that of pluripotency. These data support prior speculation that BLVRB may utilize alternative substrate(s) for its redox coupling and antioxidant effect (s) [39]; indeed, our computational network model places FMN most proximate to BLVRB (Figure 2), although additional yet-to-be substrates cannot be excluded.

Energy metabolism switches from glycolysis to oxidative phosphorylation with cellular differentiation, although preferential reliance on glycolytic pathways is a common bioenergetic feature of PSCs despite low efficient ATP generation [1,5]. The glutamine bioenergetic defect was largely reversible using glucose as a substrate, and indeed, there was striking nearly 10-fold increased accumulation of the rate-limiting hexokinase metabolite G6P in $BLVRB^{-/-}$ PSCs, consistent with enhanced glycolysis for bioenergetics or for redox homeostasis through PPP. Expectedly, both PSC proliferation and EB formation were inhibited by the glycolytic pathway inhibitor 2-DG irrespective of *BLVRB* expression, highlighting functional importance of the adaptive glycolytic phenotype known to accompany pluripotency reprogramming [1]. Interestingly, dichotomous results were seen in the presence of PPP inhibition, the bifurcating arm of the glycolytic pathway largely responsible for generation of NADPH reducing equivalents and ribose-5-phosphate that is required during riboneogenesis [23]. Indeed, studies in *Saccharomyces cerevisiae* suggest that a thermodynamically driven route of ribose production may be uncoupled from NADPH generation contingent on cellular requirements, an observation that may explain the differential sensitivity to 6-AN during proliferative vs. early-stage EB formation, whose size defines the critical first developmental stage regulating lineage fate [30,31]. Furthermore, the

observation that *BLVRB*$^{-/-}$ EB formation displayed enhanced 6-AN sensitivity suggests that BLVRB plays a requisite role in providing PPP support during early stages of EB formation-associated lineage fate potential. BLVRB preferentially uses NADPH for its redox coupling [21], although its ability to directly regulate cellular NADPH levels is unestablished. Alternatively, BLVRB-regulated PPP support could be mediated by glutamine's function as a nitrogen donor for purine/pyrimidine bases during the biosynthetic transition to multicellular growth and differentiation. While the precise mechanism remains under investigation, our data suggest that glycolytic and PPP pathways maintain requisite functions in proliferative capacity of PSCs independently of glutamine anaplerotic functions, although early stages of lineage fate potential require glutamine anaplerotic functions and an intact PPP pathway which is, in part, regulated by BLVRB activity.

Intracellular levels of α-KG maintain the pluripotency of embryonic stem cells, and diminished levels are sufficient to regulate chromatin modifications including histone methylation and PSC fate [25]. The diminished α-KG levels in *BLVRB*-deficient PSCs establish that BLVRB expression and function is responsible for the maintenance of the intracellular α-KG pool. Indeed, *BLVRB*-deficient PSCs demonstrate striking down-regulation of the histone cluster family member *HIST1H4F*, consistent with the initiation of an epigenetic switch in the transition towards lineage commitment. Previous data have demonstrated that glutamine-supported nucleotide biosynthesis is required for hematopoietic (erythroid) lineage specification, with a shift to myelomonocytic differentiation in the setting of limiting glutamine [6]. Interestingly, *BLVRB* transcript demonstrates ~40-fold induction during erythropoiesis and a restricted expression during early stages of megakaryocytopoiesis [18]. These collective observations provide a metabolic mechanism whereby BLVRB-regulated glutamine metabolism during critical stages of HSC development could modulate lineage fate unrelated to its redox-regulated antioxidant function.

Supplementary Material

Refer to Web version on PubMed Central for supplementary material.

Acknowledgements

We thank Wan-yi Yen for assistance with image capture and analysis, Irina Zaitseva for protoeomic studies, Emily Montal for assistance with ^{13}C tracing analyses, and Christian Ruiz for assistance with oxygen consumption and ^{13}C tracing analyses.

Funding

This work was supported by grants from the National Institutes of Health NIH/NCRR 1 S10 RR023680-1 (to the Stony Brook Proteomics Facility); NIH/HL091939 (W.F.B.); NIH/HL129545 (N.M.N.), NIH/AG059277 (D.V.G.), and the New York State Stem Cell Foundation (C026716, to W.F.B.). CRISPR plasmid pSpCas9(BB)-2A-GFP (PX458) was provided by F.Z.

Abbreviations

α-KG	α-ketoglutarate
2-DG	2-deoxyglucose

6-AN	6-aminonicotinamide
ALAS	aminolevulinic acid synthase
BR	bilirubin
BV	biliverdin
CCCP	carbonyl cyanide *m*-chlorophenyl hydrazine
CRISPR	clustered regularly interspaced short palindromic repeats
EB	embryoid body
ETC	electron transport chain
FH	fumarate hydratase
FMN	flavin mononucleotide
GFP	green fluorescent protein
G6P	glucose-6-phosphate
Glc	glucose
Gln	glutamine
gRNA	guide RNA
HMOX	heme oxygenase
HSC	hematopoietic stem cells
OCR	oxygen consumption rates
PAM	protospacer-adjacent motif
PSC	pluripotent stem cells
PPP	pentose phosphate pathway
redox	oxidation/reduction
ROS	reactive oxygen species
sgRNA	single-guide RNA
SpCas9	*Streptococcus pyogenes* Cas9
TCA	tricarboxylic acid
TMRE	tetramethylrhodamine ethyl ester

References

1. Zhang J, Nuebel E, Daley GQ, Koehler CM and Teitell MA (2012) Metabolic regulation in pluripotent stem cells during reprogramming and self-renewal. Cell Stem Cell 11, 589–595 10.1016/j.stem.2012.10.005 [PubMed: 23122286]
2. Owusu-Ansah E and Banerjee U (2009) Reactive oxygen species prime Drosophila haematopoietic progenitors for differentiation. Nature 461, 537–541 10.1038/nature08313 [PubMed: 19727075]
3. Balaban RS, Nemoto S and Finkel T (2005) Mitochondria, oxidants, and aging. Cell 120, 483–495 10.1016/j.cell.2005.02.001 [PubMed: 15734681]
4. Tohyama S, Fujita J, Hishiki T, Matsuura T, Hattori F, Ohno R et al. (2016) Glutamine oxidation is indispensable for survival of human pluripotent stem cells. Cell Metab. 23, 663–674 10.1016/j.cmet.2016.03.001 [PubMed: 27050306]
5. Wise DR and Thompson CB (2010) Glutamine addiction: a new therapeutic target in cancer. Trends Biochem. Sci. 35, 427–433 10.1016/j.tibs.2010.05.003 [PubMed: 20570523]
6. Oburoglu L, Tardito S, Fritz V, de Barros SC, Merida P, Craveiro M et al. (2014) Glucose and glutamine metabolism regulate human hematopoietic stem cell lineage specification. Cell Stem Cell 15, 169–184 10.1016/j.stem.2014.06.002 [PubMed: 24953180]
7. Locasale JW and Cantley LC (2011) Metabolic flux and the regulation of mammalian cell growth. Cell Metab. 14, 443–451 10.1016/j.cmet.2011.07.014 [PubMed: 21982705]
8. Gozzelino R, Jeney V and Soares MP (2010) Mechanisms of cell protection by heme oxygenase-1. Annu. Rev. Pharmacol. Toxicol. 50, 323–354 10.1146/annurev.pharmtox.010909.105600 [PubMed: 20055707]
9. Ducker GS and Rabinowitz JD (2017) One-carbon metabolism in health and disease. Cell Metab. 25, 27–42 10.1016/j.cmet.2016.08.009 [PubMed: 27641100]
10. Stocker R, Yamamoto Y, McDonagh AF, Glazer AN and Ames BN (1987) Bilirubin is an antioxidant of possible physiological importance. Science 235, 1043–1046 10.1126/science.3029864 [PubMed: 3029864]
11. Baranano DE, Rao M, Ferris CD and Snyder SH (2002) Biliverdin reductase: a major physiologic cytoprotectant. Proc. Natl Acad. Sci. U.S.A. 99, 16093–16098 10.1073/pnas.252626999 [PubMed: 12456881]
12. Cunningham O, Gore MG and Mantle TJ (2000) Initial-rate kinetics of the flavin reductase reaction catalysed by human biliverdin-IXβ reductase (BVR-B). Biochem. J. 345(Pt 2), 393–399 10.1042/bj3450393 [PubMed: 10620517]
13. Franklin EM, Browne S, Horan AM, Inomata K, Hammam MAS, Kinoshita H et al. (2009) The use of synthetic linear tetrapyrroles to probe the verdin sites of human biliverdin-IXα reductase and human biliverdin-IXβ reductase. FEBS J. 276, 4405–4413 10.1111/j.1742-4658.2009.07148.x [PubMed: 19614742]
14. Pereira PJB, Macedo-Ribeiro S, Parraga A, Perez-Luque R, Cunningham O, Darcy K et al. (2001) Structure of human biliverdin IXbeta reductase, an early fetal bilirubin IXβ producing enzyme. Nat. Struct. Biol. 8, 215–220 10.1038/84948 [PubMed: 11224564]
15. Xu F, Quandt KS and Hultquist DE (1992) Characterization of NADPH-dependent methemoglobin reductase as a heme-binding protein present in erythrocytes and liver. Proc. Natl Acad. Sci. U.S.A. 89, 2130–2134 10.1073/pnas.89.6.2130 [PubMed: 1549573]
16. Kutty RK and Maines MD (1981) Purification and characterization of biliverdin reductase from rat liver. J. Biol. Chem. 256, 3956–3962 PMID: 7217067 [PubMed: 7217067]
17. Frezza C, Zheng L, Folger O, Rajagopalan KN, MacKenzie ED, Jerby L et al. (2011) Haem oxygenase is synthetically lethal with the tumour suppressor fumarate hydratase. Nature 477, 225–228 10.1038/nature10363 [PubMed: 21849978]
18. Wu S, Li Z, Gnatenko DV, Zhang B, Zhao L, Malone LE et al. (2016) BLVRB redox mutation defines heme degradation in a metabolic pathway of enhanced thrombopoiesis in humans. Blood 128, 699–709 10.1182/blood-2016-02-696997 [PubMed: 27207795]
19. Gnatenko DV, Zhu W, Xu X, Samuel ET, Monaghan M, Zarrabi MH et al. (2010) Class prediction models of thrombocytosis using genetic biomarkers. Blood 115, 7–14 10.1182/blood-2009-05-224477 [PubMed: 19773543]

20. Antonchuk J (2013) Formation of embryoid bodies from human pluripotent stem cells using AggreWell™ plates. Methods Mol. Biol. 946, 523–533 10.1007/978-1-62703-128-8_32 [PubMed: 23179853]
21. Chu W-T, Nesbitt NM, Gnatenko DV, Li Z, Zhang B, Seeliger MA et al. (2017) Enzymatic activity and thermodynamic stability of biliverdin IXβ reductase are maintained by an active site serine. Chem. Eur. J. 23, 1891–1900 10.1002/chem.201604517 [PubMed: 27897348]
22. Hsu PD, Scott DA, Weinstein JA, Ran FA, Konermann S, Agarwala V et al. (2013) DNA targeting specificity of RNA-guided Cas9 nucleases. Nat. Biotechnol. 31, 827–832 10.1038/nbt.2647 [PubMed: 23873081]
23. Clasquin MF, Melamud E, Singer A, Gooding JR, Xu X, Dong A et al. (2011) Riboneogenesis in yeast. Cell 145, 969–980 10.1016/j.cell.2011.05.022 [PubMed: 21663798]
24. Panopoulos AD, Yanes O, Ruiz S, Kida YS, Diep D, Tautenhahn R et al. (2012) The metabolome of induced pluripotent stem cells reveals metabolic changes occurring in somatic cell reprogramming. Cell Res. 22, 168–177 10.1038/cr.2011.177 [PubMed: 22064701]
25. Carey BW, Finley LW, Cross JR, Allis CD and Thompson CB (2015) Intracellular α-ketoglutarate maintains the pluripotency of embryonic stem cells. Nature 518, 413–416 10.1038/nature13981 [PubMed: 25487152]
26. Divakaruni AS, Paradyse A, Ferrick DA, Murphy AN and Jastroch M (2014) Analysis and interpretation of microplate-based oxygen consumption and pH data. Methods Enzymol. 547, 309–354 10.1016/B978-0-12-801415-8.00016-3 [PubMed: 25416364]
27. Zhang J, Khvorostov I, Hong JS, Oktay Y, Vergnes L, Nuebel E et al. (2016) UCP2 regulates energy metabolism and differentiation potential of human pluripotent stem cells. EMBO J. 35, 899 10.15252/embj.201694054 [PubMed: 27084758]
28. Hensley CT, Wasti AT and DeBerardinis RJ (2013) Glutamine and cancer: cell biology, physiology, and clinical opportunities. J. Clin. Invest. 123, 3678–3684 10.1172/JCI69600 [PubMed: 23999442]
29. Lange K and Proft ER (1970) Inhibition of the 6-phosphogluconate dehydrogenase in the rat kidney by 6-aminonicotinamide. Naunyn. Schmiedebergs Arch. Pharmakol. 267, 177–180 10.1007/BF00999399 [PubMed: 4394804]
30. Hwang Y-S, Chung BG, Ortmann D, Hattori N, Moeller H-C and Khademhosseini A (2009) Microwell-mediated control of embryoid body size regulates embryonic stem cell fate via differential expression of WNT5a and WNT11. Proc. Natl Acad. Sci. U.S.A. 106, 16978–16983 10.1073/pnas.0905550106 [PubMed: 19805103]
31. Mohr JC, Zhang J, Azarin SM, Soerens AG, de Pablo JJ, Thomson JA et al. (2010) The microwell control of embryoid body size in order to regulate cardiac differentiation of human embryonic stem cells. Biomaterials 31, 1885–1893 10.1016/j.biomaterials.2009.11.033 [PubMed: 19945747]
32. Tomlinson IPM, Alam NA, Rowan AJ, Barclay E, Jaeger EEM, Kelsell D et al. (2002) Germline mutations in FH predispose to dominantly inherited uterine fibroids, skin leiomyomata and papillary renal cell cancer. Nat. Genet. 30, 406–410 10.1038/ng849 [PubMed: 11865300]
33. Fendt S-M, Bell EL, Keibler MA, Davidson SM, Wirth GJ, Fiske B et al. (2013) Metformin decreases glucose oxidation and increases the dependency of prostate cancer cells on reductive glutamine metabolism. Cancer Res. 73, 4429–4438 10.1158/0008-5472.CAN-13-0080 [PubMed: 23687346]
34. Lee Y-M, Lee G, Oh T-I, Kim BM, Shim D-W, Lee K-H et al. (2016) Inhibition of glutamine utilization sensitizes lung cancer cells to apigenin-induced apoptosis resulting from metabolic and oxidative stress. Int. J. Oncol. 48, 399–408 10.3892/ijo.2015.3243 [PubMed: 26573871]
35. Miralem T, Hu Z, Torno MD, Lelli KM and Maines MD (2005) Small interference RNA-mediated gene silencing of human biliverdin reductase, but not that of heme oxygenase-1, attenuates arsenite-mediated induction of the oxygenase and increases apoptosis in 293A kidney cells. J. Biol. Chem. 280, 17084–17092 10.1074/jbc.M413121200 [PubMed: 15741166]
36. Kapitulnik J and Maines MD (2009) Pleiotropic functions of biliverdin reductase: cellular signaling and generation of cytoprotective and cytotoxic bilirubin. Trends Pharmacol. Sci. 30, 129–137 10.1016/j.tips.2008.12.003 [PubMed: 19217170]

37. Yamaguchi T and Nakajima H (1995) Changes in the composition of bilirubin-IX isomers during human prenatal development. Eur. J. Biochem. 233, 467–472 10.1111/j.1432-1033.1995.467_2.x [PubMed: 7588789]

38. Mourino S, Giardina BJ, Reyes-Caballero H and Wilks A (2016) Metabolite-driven regulation of heme uptake by the biliverdin IXβ/δ-selective heme oxygenase (HemO) of Pseudomonas aeruginosa. J. Biol. Chem. 291, 20503–20515 10.1074/jbc.M116.728527 [PubMed: 27493207]

39. McDonagh AF (2001) Turning green to gold. Nat. Struct. Biol. 8, 198–200 10.1038/84915 [PubMed: 11224558]

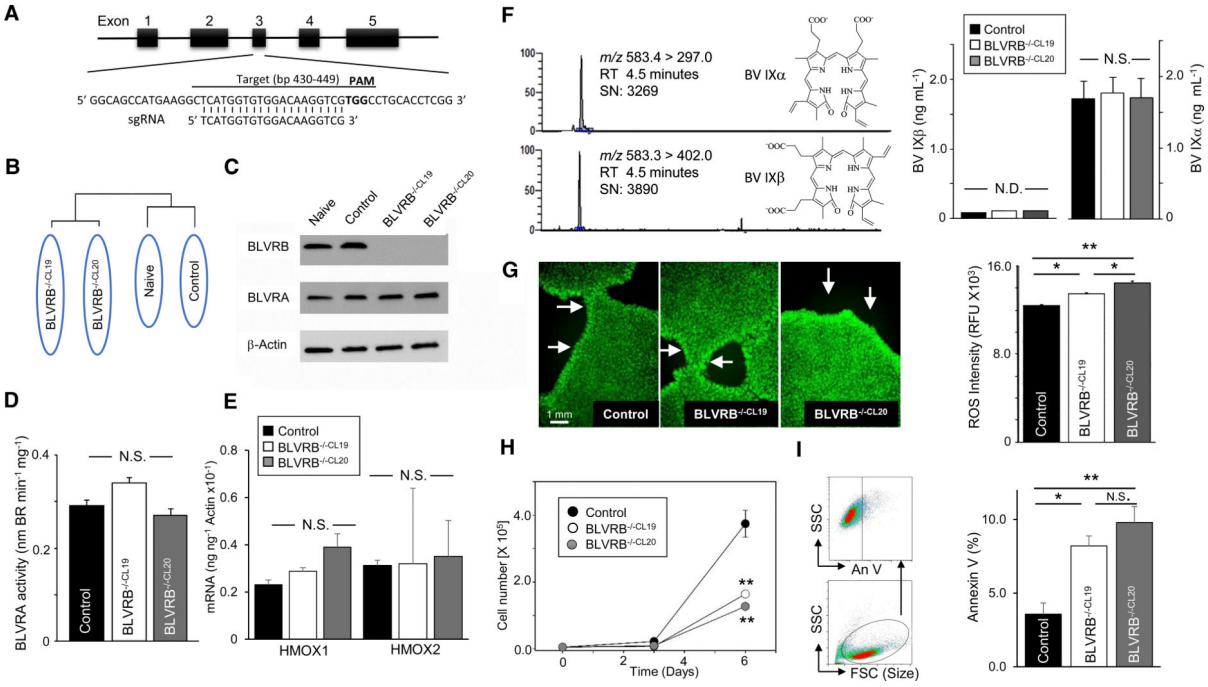

Figure 1. Generation and characterization of *BLVRB*$^{-/-}$ PSCs.

(**A**) BLVRB intron/exon schema is shown with the nucleotide sequence of sgRNA (430–449 bp) situated upstream of the 3-bp PAM (bold). (**B**) Cluster dendogram using the subset of differentially expressed genes ($N = 42$, $P \leq 0.001$). (**C**) Immunoblot using PSC lysates (10 μg/lane) detected with anti-BLVRB, anti-BLVRA, and anti-Actin antibodies. (**D**) BLVRA activity was determined using 100 μg of PSC-solubilized lysates and BV IXα as a substrate; data are expressed as mean (nm bilirubin min^{-1} mg^{-1}) ± SEM ($N = 3$). (**E**) *HMOX1* and *HMOX2* mRNA levels using 50 ng of total cellular RNA (triplicate determinations normalized to *β-actin* mRNA, mean ± SEM). (**F**) PSCs (1×10^6/well) were grown until confluent at which time the media was changed for 24 h quantification of secreted BV IXα and BV IXβ isomers by LC–MS/MS and multiple reaction monitoring; shown are the *m/z* spectra, retention time (RT), and signal-to-noise (SN) ratio for the individual isomers. Normalized isomeric quantifications are displayed to the right (mean ± SEM, $N = 3$). (**G**) PSCs were propagated until 70% confluent and ROS accumulation was quantified after 30 min labeling using CellRox green; images were acquired under identical conditions using confocal microscopy and cellular intensity was quantified using Image J software; data are presented as the mean ± SEM ($N > 750$ cells/sample) from one representative experiment repeated on two distinct occasions; arrows highlight the enhanced leading edge ROS accumulation (scale bar is shown). (**H** and **I**) Growth curves (**H**) and flow cytometric quantification of Day 6 Annexin V (An V) binding using gates as shown in accompanying scatter grams (**I**; SSC side scatter; FSC forward scatter); results are mean ± SEM, $N = 3$ wells from a representative experiment repeated once. For all panels, *$P < 0.05$; **$P < 0.01$; N.S., not significant; N.D., not detected.

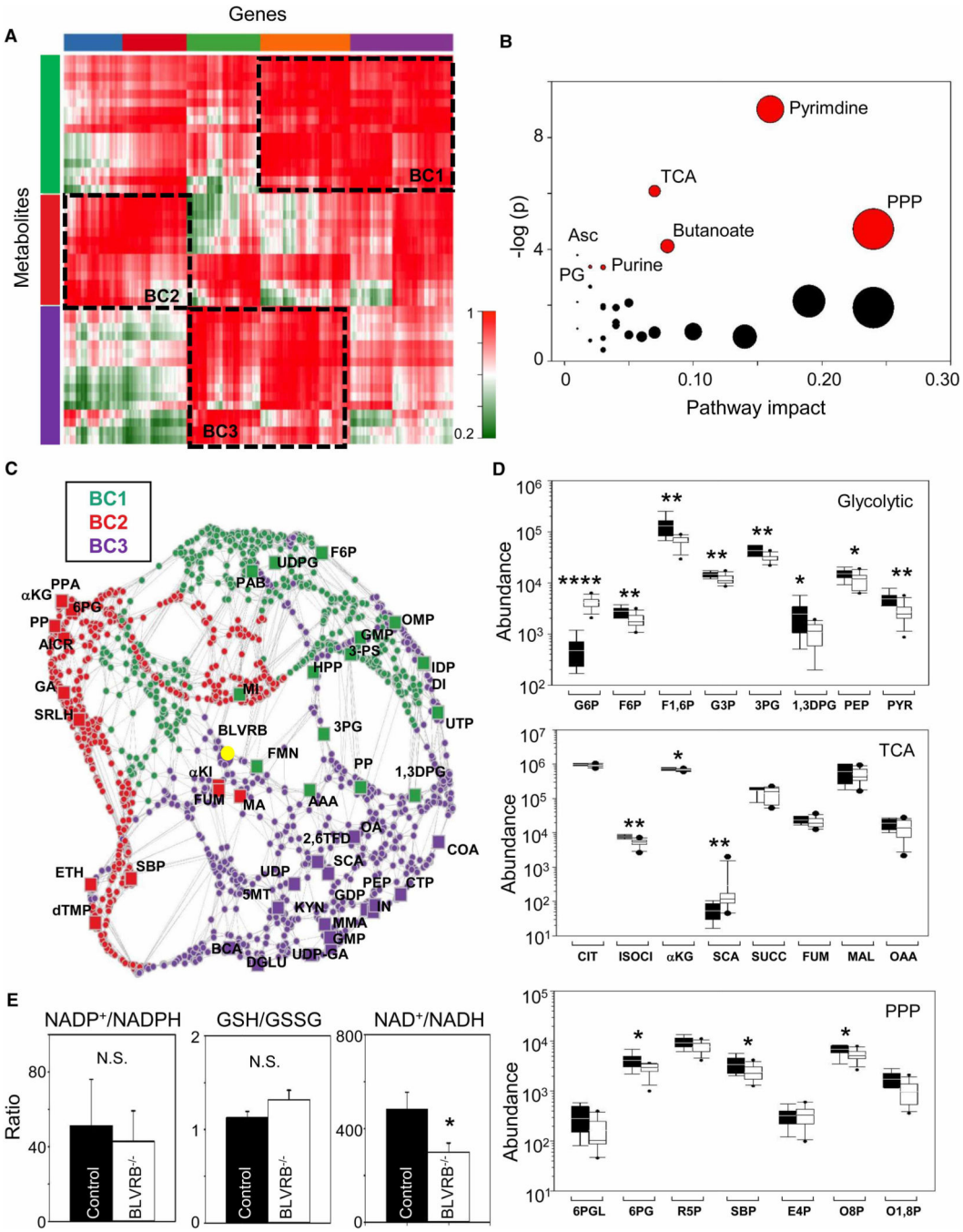

Figure 2. Computational studies identify *BLVRB*-regulated gene/metabolic networks.

(**A**) Unsupervised hierarchical clustering of gene/metabolite pairs was completed based on the correlations between those genes ($N = 1932$) and metabolites ($N = 45$) highly correlated with *BLVRB* expression across the four PSC genotypes (naive, control, $BLVRB^{-/-CL19}$ and $BLVRB^{-/-CL20}$; Pearson coefficient $r \geq 0.8$). The clustering algorithm defined five gene groups (blue, red, green, orange, and purple) and three metabolite groups (green, brown, and purple), delimited into three highly correlated biclusters BC1, BC2, and BC3 ($P < 2.2 \times 10^{-16}$); correlation scale bar is shown. (**B**) Pathway analysis plot was generated from

BLVRB-associated metabolites ($n = 45$); enriched pathways with adjusted Holm–Bonferroni *P*-values <0.05 are highlighted in red; larger circles are predicted to have a greater impact on PSC function; TCA: tricarboxylic acid; PPP: pentose phosphate pathway; Asc: ascorbate and aldarate metabolism; PG: pentose/glucoronate interconversions. (**C**) BLVRB network plot comprises 1977 nodes and 11 300 edges depict connectivity of genes (circles) and metabolites (squares), delimited by bicluster (*BLVRB* is highlighted by yellow circle); metabolite abbreviations are available in Supplementary Table S2. (**D**) Metabolite abundance data for discrete pathways comparing control ($N = 6$) vs. $BLVRB^{-/-}$ ($N = 12$) PSCs (aggregate data for $BLVRB^{-/-CL19}$ and $BLVRB^{-/-CL20}$); box plots represent the within-group interquartile range encompassing 50% of the values, while the horizontal bar within each box represents the group mean (95% confidence intervals and outliers are depicted). (**E**) Redox ratios for $NADP^+$/NADPH, GSH/GSSG (reduced/oxidized glutathione), and NAD^+/NADH are presented as mean ± SEM from control ($N = 6$) or aggregate $BLVRB^{-/-}$ PSCs ($N = 12$); (**D** and **E**) $^*P < 0.05$; $^{**}P < 0.01$; $^{****}P < 0.0001$.

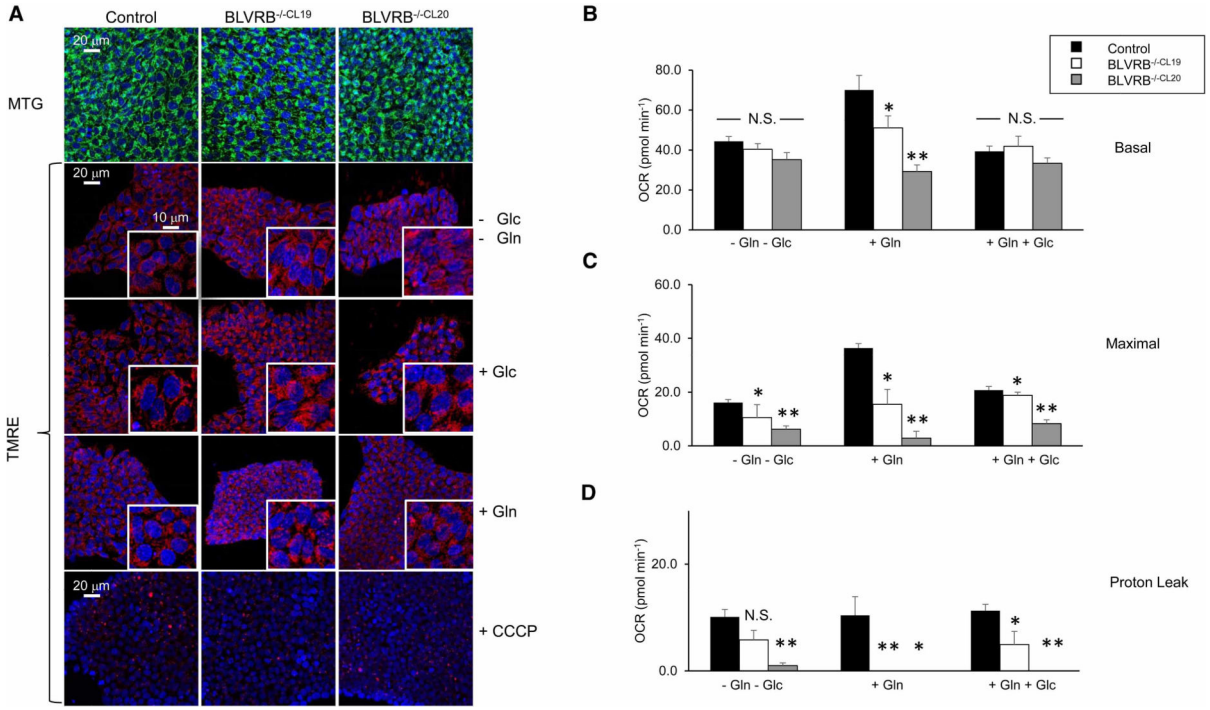

Figure 3. Bioenergetic defects in *BLVRB*-deficient stem cells.

(**A**) Cells were grown in mTesR media until ~70% confluence, followed by MitoTracker (MTG) staining (*upper panels*), or switched to DMEM (with or without 2 mmol l^{-1} glutamine or 10 mmol l^{-1} glucose) in the presence of 100 nM TMRE for confocal microscopy [for some experiments, cells were incubated for 60 s with the protonophore CCCP (10 μM l^{-1}) prior to image capture]; nuclei (blue) are visualized using DAPI and scale bars are shown. (**B–D**) Cells (2.0×10^4/well) were evenly seeded into mTeSR media and grown until confluent, followed by 3 h equilibration in unbuffered XF basal media supplemented (or not) with 2 mmol l^{-1} glutamine and/or 10 mmol l^{-1} glucose for determinations of basal and maximal respiration (**B** and **C**), or proton-leaked respiration (**D**); data are presented as mean ± SEM ($N = 8$ wells) from a representative experiment, repeated twice; *$P < 0.05$; **$P < 0.01$; N.S., not significant.

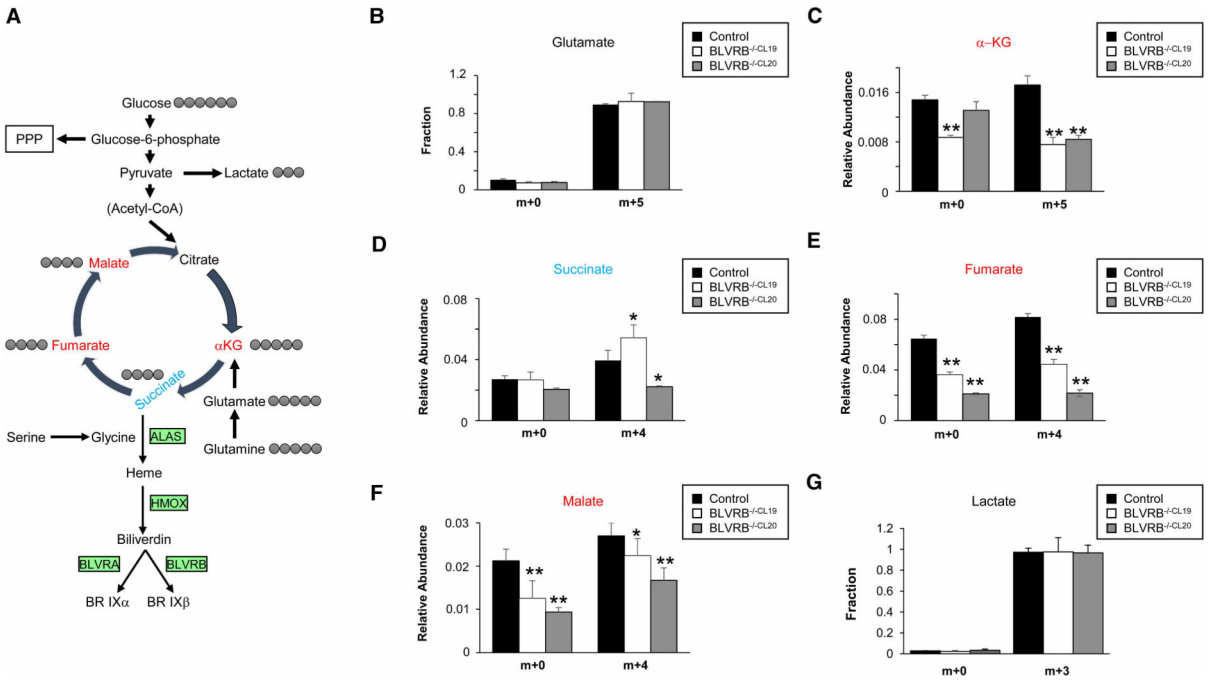

Figure 4. Glutamine-restricted TCA defect in *BLVRB*-deficient stem cells.

(**A**) Schema outlining critical BLVRB-regulated pathways (PPP, glycolytic, and TCA) intersecting with heme generation/degradation pathways (key enzymatic reactions in green-shaded boxes), along with glucose- and glutamine-derived TCA carbon atom transition map for key intermediates (gray circles); PPP: pentose phosphate pathway; ALAS: rate-limiting aminolevulinic acid synthase; HMOX: heme oxygenase. (**B–F**) Fractional labeling using [U5-$^{13}C_5$] glutamine (**B–F**) or [U6-$^{13}C_6$] glucose (**G**) was determined for key TCA cycle intermediates at 3 h, and data presented as mean ± SEM (N = 3 wells) from a representative experiment, repeated twice; *P < 0.05; **P < 0.01.

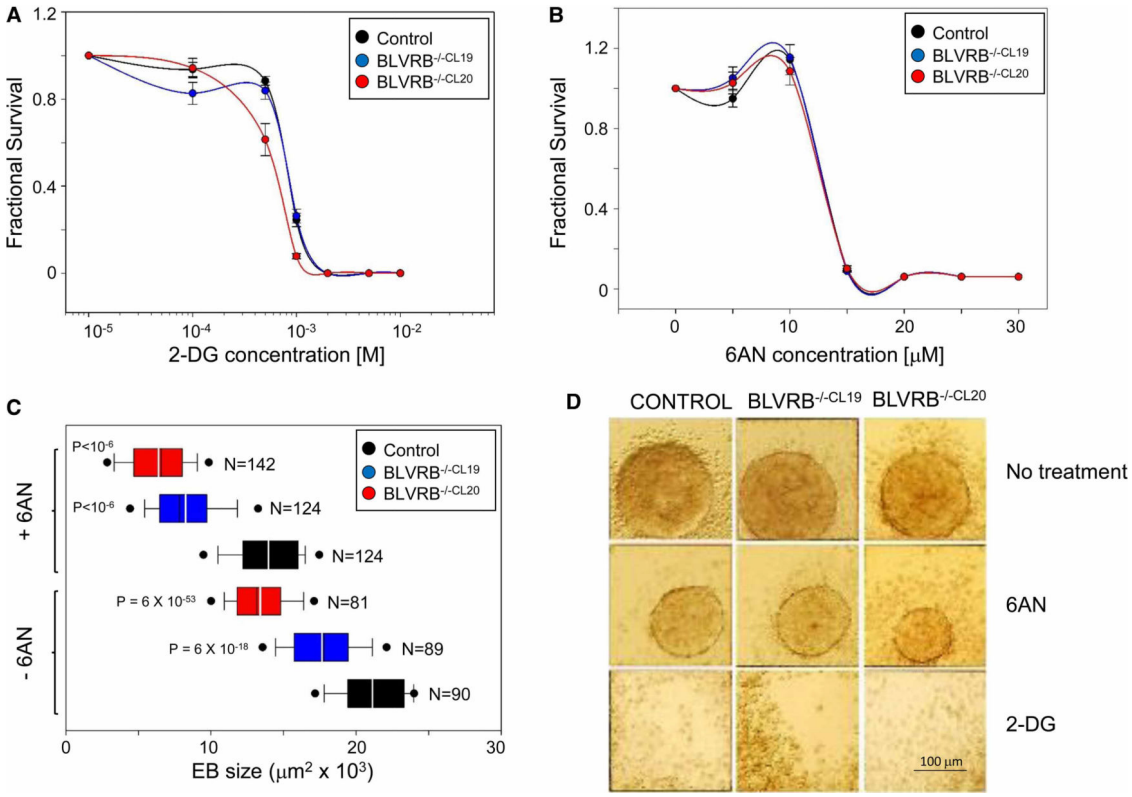

Figure 5. BLVRB-regulated glycolytic and PPP pathway functions.

(**A** and **B**) PSCs (1×10^4) were supplemented every 2 days with varying concentrations of the glycolytic pathway inhibitor 2-DG (A) or the PPP pathway inhibitor 6-AN (**B**), followed by cell quantification at Day 6. Data are from a single representative experiment (replicated twice) and presented as fractional survival compared with Day 0 (mean ± SEM, $N = 3$ wells). (**C**) EB size was quantified in three-dimenstional AggreWell plates at Day 3, using cells (1×10^5/well) lacking inhibitors or preincubated with 50 μM 6-AN or 0.5 mM 2-DG. Surface area (two-dimensional) was quantified using Image J software (EB numbers/genotype are provided), and sizes are presented as mean ± SEM from a single representative experiment, repeated twice. Note that EBs were not evident in any 2-DG-treated genotypes; for baseline comparisons, *P*-values were determined using one-tailed t-test, while bootstrap resampling was used to quantify relative percent size change in the presence of 6-AN; note that while the relative size changes for *BLVRB*$^{-/-CL19}$ and *BLVRB*$^{-/-CL20}$ are not significantly different, the percent change in each is greater than control (*P*-value < 0.000001). (**D**) Representative EB microscopic images with or without 50 μM 6-AN or 0.5 mM 2-DG; scale bar is shown.